metals

MDPI

Article

The Effect of Heat Treatment on the Oxidation Resistance of Cobalt-Based Superalloys

James P. Moffat [1], Tamsin E. Whitfield [1], Katerina A. Christofidou [2], Ed J. Pickering [3], Nicholas G. Jones [1] and Howard J. Stone [1,*]

[1] Department of Materials Science and Metallurgy, University of Cambridge, 27 Charles Babbage Road, Cambridge CB30FS, UK; jpm208@cam.ac.uk (J.P.M.); tw398@cam.ac.uk (T.E.W.); ngj22@cam.ac.uk (N.G.J.)
[2] Department of Materials Science and Engineering, Sir Robert Hadfield Building, Mappin Street, Sheffield S1 3JD, UK; k.christofidou@sheffield.ac.uk
[3] Department of Materials, University of Manchester, Oxford Road, Manchester M13 9PL, UK; ed.pickering@manchester.ac.uk
* Correspondence: hjs1002@cam.ac.uk; Tel.: +44-(0)1223-334320

Received: 5 January 2020; Accepted: 10 February 2020; Published: 12 February 2020

Abstract: Degradation of the mechanical integrity of cobalt-based superalloys can occur as the carbide network is progressively oxidised during high temperature service. In this study, a heat-treatment aimed at redistributing the carbides was tested on two similar commercial Co-based superalloys, one with high C content (Co-101) and one with low C content (Stellite-21), to determine its influence on oxidation resistance. It was found that the carbide phases in the lower C-containing alloy could be solutioned more readily than the higher C-containing alloy, enabling the continuity of the carbide network to be reduced. This resulted in a reduced attack of the carbides down the interdendritic channels during oxidation testing, but increased thickness of the oxide overscale.

Keywords: cobalt-based superalloys; heat treatment; oxidation

1. Introduction

Co-based superalloys find use in a range of applications that require high mechanical strength in addition to good wear [1–3] and corrosion resistance [4–7] at temperatures beyond 1000 °C [8,9]. Such applications include components in gas turbine engines [10] and processing equipment in molten glass vitrification [11]. The excellent properties of Co-based superalloys originate from microstructures that contain a continuous solid solution strengthened matrix reinforced by inter-, and intra-granular carbides. To minimise issues with alloy hardness during machining [12], investment casting procedures are typically utilised to obtain near-net shape components [13]. This processing route results in dendritic microstructures with continuous carbide networks located at the interdendritic regions. Since these carbide networks provide the necessary mechanical strengthening for most industrial applications, it is common for components to be serviced in their as-cast state, without additional heat treatments.

A major disadvantage of the continuous carbide networks is the uninterrupted pathways they provide for preferential oxidation and corrosion. Such attack typically initiates at the intersection of the carbide network with the surface, leading to the formation of pits [5]. In order to achieve environmental resistance through the formation of a passivating external Cr_2O_3 scale, Co-based superalloys typically contain 20–30 wt.% Cr [14,15]. The Cr may also facilitate the formation of the carbide network [16]. However, it has been previously shown that Cr-based carbides may be preferentially oxidised below the external Cr_2O_3 scale, particularly in applications such as molten glass vitrification [17]. Since Cr carbides are the primary strengthening phases in Co-based

superalloys [15], their loss through oxidation can result in significant deterioration of mechanical properties, leading to crack initiation and propagation [18]. This degradation may be exacerbated in situations with high-velocity gas streams or liquid flows.

A number of strategies have been investigated to mitigate the problems associated with oxidation and corrosion in Co-based superalloys. In work by Di Martino et al. [17,19] electrochemical oxidation of a variety of alloys was performed to establish compact and adherent passivating layers before the alloys were exposed to the corrosive environment. Whilst this strategy successfully improved the corrosion resistance, oxygen diffusion through the Cr_2O_3 scale still led to oxidation of the sub-surface carbide networks. Furthermore, abrasive conditions were shown to quickly denude the surface of the protective scale, leading to further oxidation and corrosion.

Improvements in environmental resistance have also been sought through modification of alloy chemistry. In this regard, a common approach to increasing environmental resistance has been through addition of so-called "active elements". For example, addition of Y has been reported to increase the adherence of oxide scales at intermediate temperatures [20]. Similarly, Mn has been observed to increase oxidation resistance by stabilising Cr_2O_3 and Al_2O_3 scales [21]. It has also been shown that benefits to oxidation resistance may be derived through incorporation of Hf to form more resilient refractory metal carbides [22,23]. Whilst initial results appear encouraging, particularly for the high temperature morphological stability and creep resistance of HfC-containing alloys, research is still required to identify the elemental additions that provide optimal environmental resistance without compromising mechanical performance. An alternative strategy to improve oxidation resistance is to break-up the continuity of the carbide network through microstructural modification, as this limits the depth to which preferential attack may occur into the alloy. However, this approach has yet to be pursued and reported in the literature.

In this study, the efficacy of microstructural modification by heat treatment for improving environmental resistance has been evaluated. Two Co-based superalloys with similar compositions but differing C concentrations covering the range found in commercial alloys were studied, Co-101 (high C content) and Stellite-21 (low C content). The benefits obtained were quantified through measurements of oxidation attack depth and limitations set by the C content were identified.

2. Materials and Methods

Two commercial Co-based alloys with closely related compositions: Co-101 (high C content) and Stellite-21 (low C content) were investigated. The nominal compositions of these alloys are given in Table 1 along with actual compositions determined by energy dispersive X-ray spectroscopy (EDX). Co-101 was investment cast and supplied in the as-cast state and contained a dendritic, coarse-grained microstructure. Stellite-21 was obtained in the form of 5 mm diameter welding rods that were subsequently vacuum induction re-melted in a Balzers VSG 02 (Balzers, Balzers, Oberland, Liechtenstein) with a Balzers TPG 300 pressure controller to produce a larger cast ingot with a comparable dendritic microstructure to the Co-101 material. To study the influence of heat treatment, sections of each alloy were sealed in quartz ampoules under an argon atmosphere and solution heat treated at 1250 °C for 10 h followed by a quench into iced water.

Table 1. Nominal and actual (determined by EDX) compositions of alloys Co-101 and Stellite-21.

Alloy			Co	Cr	Ni	Mo	Fe	Si	Mn	C	W
Co-101	Nominal	(wt.%)	Bal.	30.0	10.0	5.00	3.00	0.600	0.500	0.500	-
		(at.%)	Bal.	32.4	9.57	2.93	3.02	1.20	0.511	2.34	-
	EDX	(wt.%)	Bal.	33.86	9.87	4.89	1.15	0.72	0.63	-	-
		(at.%)	Bal.	37.06	9.56	2.90	1.18	1.45	0.66	-	-
Stellite-21	Nominal	(wt.%)	Bal.	29.0	2.80	5.30	2.00	1.00	0.700	0.280	0.400
		(at.%)	Bal.	31.6	2.70	3.13	2.03	2.02	0.723	1.32	0.123
	EDX	(wt.%)	Bal.	28.61	2.79	5.37	2.26	0.94	0.75	-	0.34
		(at.%)	Bal.	31.56	2.72	3.21	2.32	1.92	0.79	-	0.11

Isothermal oxidation testing of the alloys in the as-cast and heat-treated states was performed in laboratory air for 100 h at 1000 °C. The surfaces of each specimen were ground with progressively finer media, culminating in a 1 μm diamond polish. During oxidation testing, the samples were contained within alumina crucibles to ensure that any spalled oxide was captured and included in subsequent mass gain measurements. The masses of the samples before and after testing were determined using a XP105 DeltaRange® (Mettler Toledo, Columbus, OH, US) microbalance (accurate to +/−10 μg). On completion of the oxidation tests the samples were cross sectioned on a slow speed saw to limit damage to the oxide scales and prepared for microstructural examination using standard metallographic techniques.

Microstructural analyses were performed in a GeminiSEM 300 (Carl Zeiss Microscopy, Jena, Thuringia, Germany) scanning electron microscope (SEM). Images were acquired using backscattered electrons (BSE) and elemental analyses were performed using an 50 mm^2 X-max^N EDX silicon drift detector (Oxford Instruments, Abingdon, Oxfordshire, UK). The actual alloy compositions were determined from the average of EDX point analyses over a representative 200 × 150 μm^2 area of the microstructure. Data for C was excluded from these analyses due to the difficulty in reliably determining the concentration of this element using this method. For Co-101, it was noted that the actual Cr content was > 3 wt.% higher than the nominal value and the Fe content was 2 wt.% lower. In contrast, the actual compositions of Stellite-21 were close to their nominal values. Quantification of the area fractions of the phases present within a given microstructure were performed by image analysis from an 800 × 800 μm^2 region using the ImageJ software package (V1.52k, National Institute for Health, Bethesda, MD, US) [24].

Transmission electron microscopy (TEM) was performed on 3 mm diameter discs that had been thinned to electron transparency by twinjet electropolishing. Thinning was achieved using a 6% perchloric acid in methanol solution at −25 °C under an applied potential of 20 V. Selected area diffraction patterns (SADP) and scanning transmission electron microscopy energy dispersive X-ray spectroscopy (STEM-EDX) analyses were performed using an TALOS F200X (FEI™, Thermo Fisher Scientific, Hillsboro, OR, US) for the Co-101 specimens, and an FEI™ Tecnai Osiris for the Stellite-21 specimens, both operated at 200 kV.

Phase identification was achieved by analysing X-ray diffraction (XRD) data, collected using a D8 ADVANCE Davinci instrument (Bruker, Billerica, MA, US) fitted with a LynxEye EX position sensitive detector. The sample was illuminated by Ni-filtered Cu Kα radiation and data acquired between 20° and 100° 2θ. To improve the sampling statistics during data collection, the specimens were rotated at 30 revolutions per minute. Analysis of the diffraction data was performed using full pattern Pawley refinements within the TOPAS-Academic (V4.1, Coelho Software, Brisbane, Australia) software.

Differential scanning calorimetry (DSC) was performed using a Netzsch 404 calorimeter (NETZSCH-Gerätebau GmbH, Selb, Bavaria, Germany) with cylindrical specimens (5 mm in diameter and 1.2 mm thick) prepared by electro discharge machining. All DSC measurements were performed in alumina crucibles and under flowing argon (flow rate of 50 mL/min). Specimens were heated to 1450 °C, cooled to 1000 °C and re-heated to 1450 °C. The heating and cooling ramps were performed at a rate of 10 °C/min and between each step a 10 min isothermal hold was applied to allow the temperature of the sample to equilibrate.

3. Results and Discussion

3.1. As-Cast Co-101 Microstructure

To assess the effectiveness of the heat treatment in breaking up the continuity of the carbide network of the alloy Co-101, characterisation of the microstructure was performed in the as-cast and heat-treated state. BSE images of Co-101 in the as-cast state are shown in Figure 1.

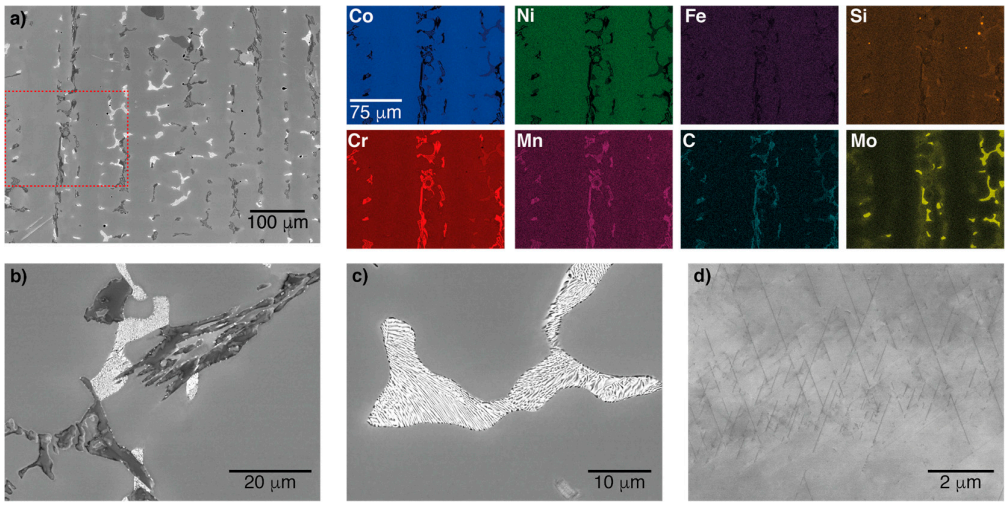

Figure 1. BSE micrographs of Co-101 in the as-cast state. (**a**) low magnification image showing the dendritic microstructure, (**b**) region containing the dark contrast M_7C_3 constituent, (**c**) region of the lamella intergrowth of the dark M_7C_3 and bright contrast $M_{23}C_6$ phases, and (**d**) the needle-like features surrounded by the γ matrix. EDX elemental distribution maps of Co, Ni, Fe, Si, Cr, Mn, C, and Mo are shown, taken from the highlighted region in (**a**).

The microstructure was comprised of grey contrast dendrites, likely to be the γ phase, with a centre-to-centre spacing of 45 μm, as well as two distinct interdendritic constituents (Figure 1a). One constituent of the interdendritic region exhibited a blocky morphology and a darker contrast compared to the γ dendrites (Figure 1b). The other constituent had an overall brighter contrast compared to all other phases, however, closer examination revealed it to be comprised of a lamellar inter-growth of bright and dark contrast phases (Figure 1c). The area fractions of the matrix phase, the dark and the bright interdendritic constituents were 93%, 4%, and 3%, respectively. Needle-like features were also observed within the γ matrix that showed distinct alignments, suggesting a strong crystallographic relationship with the surrounding material (Figure 1d). These features could be attributed to slip bands or stacking faults in the γ matrix. However, they are also consistent with the martensitically formed hexagonally closed packed (hcp), ε phase in alloys of this type [25,26]. Near the periphery of the γ dendrites a progressive variation of BSE image contrast was observed, likely to be indicative of the solidification induced-microsegregation typical of as-cast alloy microstructures. From the highlighted region in Figure 1a, the EDX composition maps indicated that the matrix phase was rich in Co, Ni and Fe, the blocky dark contrast phase was rich in Cr, C and potentially Mn (although it is noted that the Mn Kα emission energy is similar to that of Cr), and the bright contrast phase was rich in Mo and Si. The blocky dark contrast phase showed slight enrichment of Mo, and the bright contrast phase contained small quantities of Cr and C. These observations are likely to be related to partitioning of these elements during solidification. Notably, Si tends to partition to the liquid phase, leading to segregation of Si to pores and inclusions in the microstructure of the solidified alloy.

An XRD pattern obtained from Co-101 in the as-cast state is shown in Figure 2. Peaks associated with four major phases were identified. These included a face-centred cubic (fcc) phase, likely to be the γ matrix expected in alloys of this type [27,28], two hexagonal phases, and one cubic phase. Using the data obtained from the EDX elemental maps to narrow the range of possible phases forming in the material, the hexagonal carbide was identified as the Cr-rich M_7C_3 carbide, whereas the cubic carbide was found to be a Mo rich variant of the $M_{23}C_6$ carbide. Although the remaining hexagonal phase is likely to be the ε phase, further analysis would be required to definitely confirm its identity.

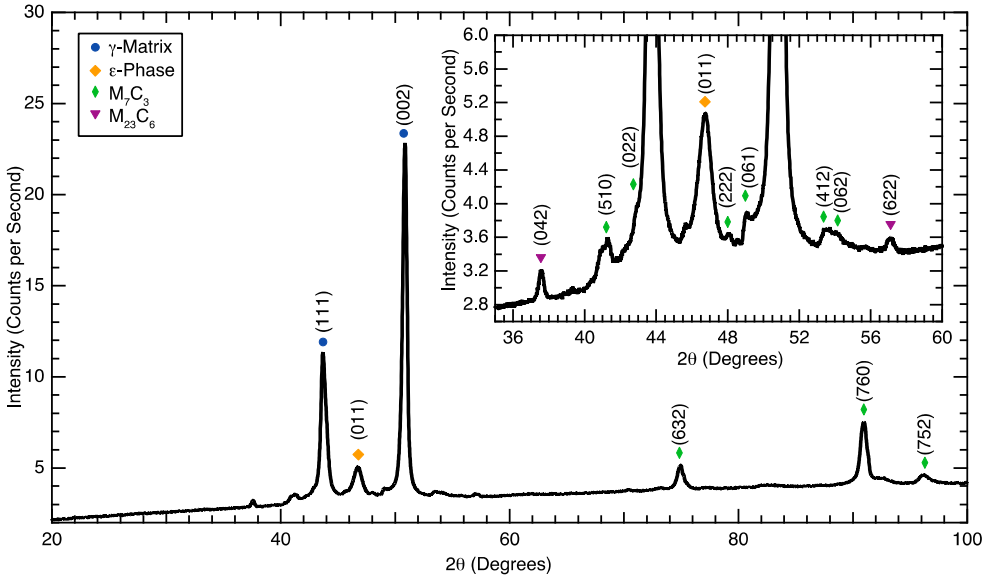

Figure 2. XRD pattern of Co-101 in the as-cast state. The key reflections from the four constituent phases have been identified using TOPAS. An inset is included highlighting the key peaks that can be seen in the range of 35°–60° 2θ.

To unambiguously determine the interdendritic constituents in Co-101, STEM imaging with EDX and SADP analyses were performed, the results of which are shown in Figure 3. From the STEM EDX elemental distribution maps three regions, (A), (B), and (C) could be clearly identified.

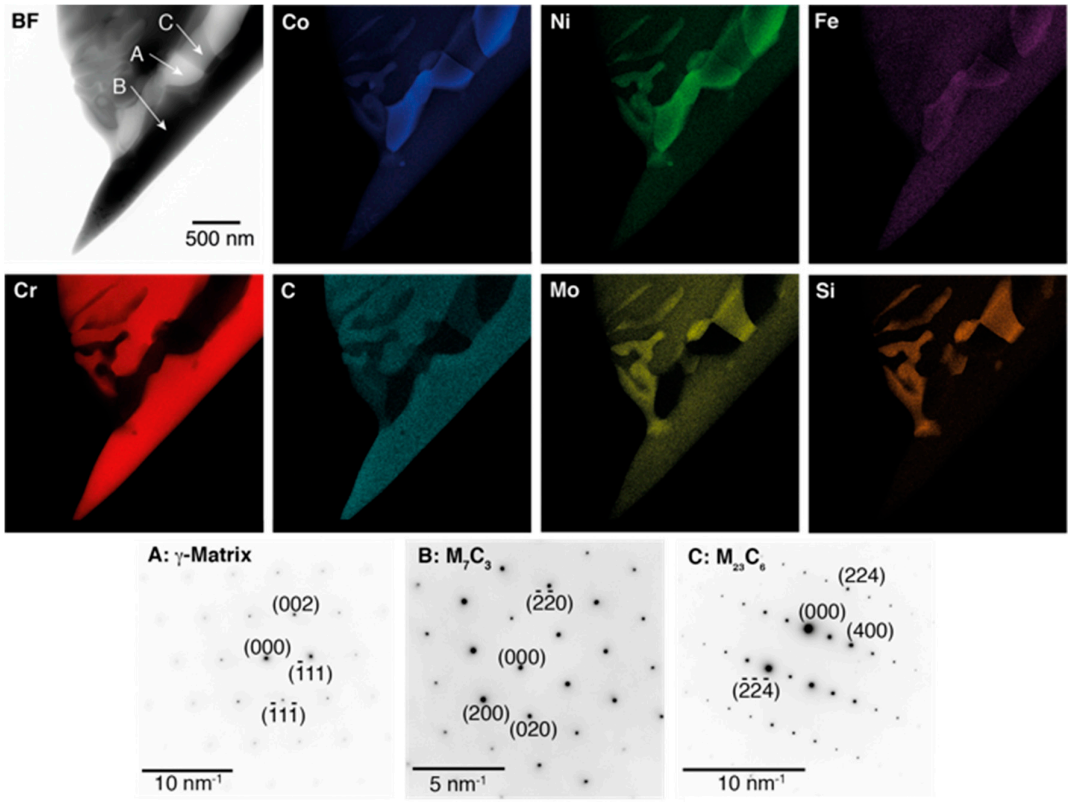

Figure 3. Bright field (BF) image of a region of interest in Co-101 with corresponding STEM-EDX elemental distribution maps of Co, Ni, Fe, Cr, C, Mo and Si. SADPs of the major phases in Co-101, labelled A, B and C in the BF image, were identified as the γ matrix, M_7C_3 and $M_{23}C_6$ with zone axes [110], [0001] and [$0\bar{8}4$], respectively.

All three regions showed similar segregation behaviour to that observed in the SEM-EDX maps in Figure 1. Region (A) showed enrichment of Co, Ni and Fe, region (B) was rich in Cr and C, with small amounts of Mo segregation and region (C) contained high concentrations of Mo, Si and C. SADPs from regions that showed high concentrations of Co, Ni and Fe were identified as having an fcc structure. This was consistent with it being the γ matrix phase. Regions with high Cr and C contents were identified as the hexagonal M_7C_3 phase and regions with high Mo, C and Si contents were identified as having a cubic structure, consistent with the $M_{23}C_6$ phase. Comparison of the BSE, SEM and STEM data enabled the darker contrast interdendritic constituent, Figure 1b, to be identified as the Cr-rich M_7C_3 phase whilst the brighter contrast lamellar intergrowth, Figure 1c, was a Mo-rich $M_{23}C_6$ phase. The Stellite alloys developed by Haynes have been shown to contain similar carbide phases, as have other alloys reported in the literature [27,29–31].

3.2. Microstructural Modification of Co-101 by Heat Treatment

With the as-cast microstructure characterised, exploration of the thermophysical properties was required to identify a suitable carbide redistribution temperature. The DSC thermogram obtained from as-cast Co-101 (black trace) is shown in Figure 4.

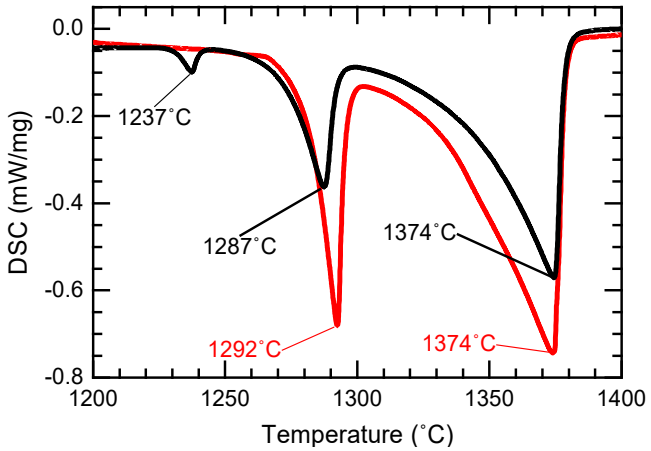

Figure 4. DSC heating traces of as-cast (black trace) and 10 h 1250 °C heat-treated Co-101 (red trace) with peak temperatures labelled.

Three endothermic peaks can be observed in the thermogram at temperatures of 1237, 1287, and 1374 °C. The first two peaks may be attributed to the melting of the two interdendritic carbide phases, whilst the last peak corresponds to bulk melting of the γ matrix dendrites. Although the area (and therefore volumetric) fractions between the two interdendritic phases are different, enthalpic variations between phases during melting will also contribute to the differences in peak area in the DSC trace. From these data a heat treatment temperature of 1250 °C was selected for partial re-solution of the carbides. This was above the first endothermic peak associated with the carbide phases but below the temperature at which significant incipient melting of the alloy would be likely to occur.

Following the heat treatment of 10 h at 1250 °C the DSC procedure was repeated, with the resulting thermogram shown as the red trace in Figure 4. Only two endothermic peaks can be observed for the heat-treated material, occurring at 1292 °C and 1374 °C, respectively. These features are similar to the two high-temperature endothermic peaks observed in the thermogram from Co-101 in the as-cast state. The absence of the 1237 °C peak observed in the as-cast DSC thermogram indicates that the 10 h heat treatment was sufficient to eliminate the phase associated with this event. In addition to the slight shift in the temperature at which the remaining carbide peak occurred, the peak was observed to be sharper following the heat treatment. This is consistent with reduction in compositional inhomogeneity of the associated phases as a result of interdiffusion of the constituent elemental species during the heat treatment.

The microstructure of Co-101 in the heat-treated state (Figure 5), exhibited several differences to that of the as-cast alloy. The Mo-rich $M_{23}C_6$ interdendritic phase, observed in the as-cast state, Figure 1b, was absent following the heat treatment, suggesting that it had been solutioned leaving only the γ matrix and the Cr-rich M_7C_3 phase. The absence of the Mo-rich $M_{23}C_6$ phase in the microstructure accompanied by the loss of the 1237 °C peak in the DSC thermogram from the heat-treated material confirms that this peak corresponded to the minority carbide phase. Changes to the morphology of the Cr-rich M_7C_3 carbide were also observed. Higher magnification imaging of the M_7C_3 phase following heat treatment, Figure 5b, showed evidence of spherodisation. This is similar to the behaviour reported for Co-Cr-Mo-C biomedical implant alloys when heat treated [32]. Whilst both spherodisation and partial solutioning of the carbide phases had occurred during the heat treatment, it is clear that these effects were insufficient to appreciably reduce the continuity of the interdendritic carbide network. Indeed, the area fractions of the phases remained similar to those of the as-cast specimen, with 95% γ phase and 5% interdendritic carbide, with the reduced carbide content being attributable to dissolution of the $M_{23}C_6$ phase. To assess the effectiveness of the heat treatment in modifying the extent of oxidation attack, material in both the as-cast and heat-treated conditions were examined after 100 h at 1000 °C in air.

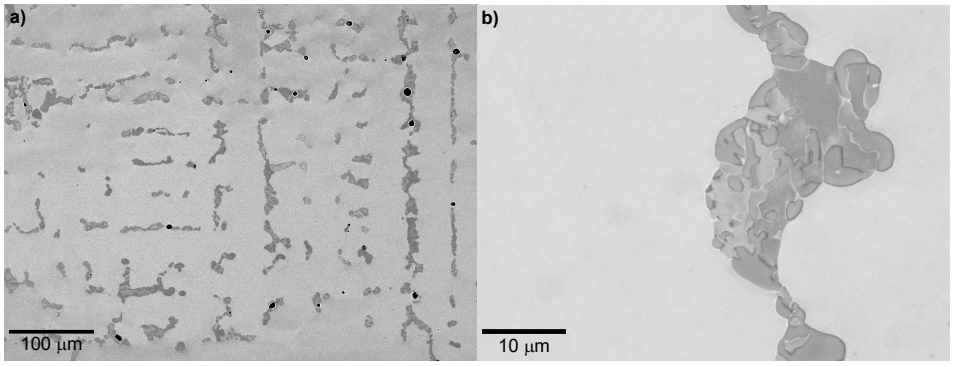

Figure 5. BSE micrographs of heat-treated Co-101, (**a**) low magnification image showing the dendritic microstructure of Co-101, (**b**), higher magnification image of the interdendritic M_7C_3 phase.

3.3. Oxidation of Co-101

Initial examination of the as-cast and heat-treated samples after oxidation at 1000 °C for 100 h revealed small amounts of spallation from the as-cast sample and moderate amounts from the heat-treated sample. The as-cast sample incurred a mass increase of 1.05 mg/cm^2 after oxidation whereas the heat-treated alloy gained an increase of 1.48 mg/cm^2. BSE images and corresponding EDX elemental concentration maps from the alloy-oxide interfaces for the as-cast and heat-treated samples are shown in Figure 6a,b respectively. In both the as-cast and heat-treated alloys, a semi-continuous Cr-rich oxide 5–6 μm thick was observed to have formed on the specimen surface.

Beneath the alloy-oxide interface, extensive oxidation of the interdendritic carbide networks could be seen, generating fissures 50 μm deep into both the as-cast and heat-treated sample surfaces. The depth of penetration was observed to be more severe in regions that had continuous carbide networks. Two oxidation products could be observed in the oxidised carbide regions from the EDX elemental maps. Near the surface, to a depth of 30 μm, the carbide regions contained Cr-rich oxides whereas Co and Si-rich oxides were found extending to a depth of 50 μm. Such behaviour was similar in both samples however, in the heat-treated specimen, Si-rich oxides were more localised to deeper regions of the fissures.

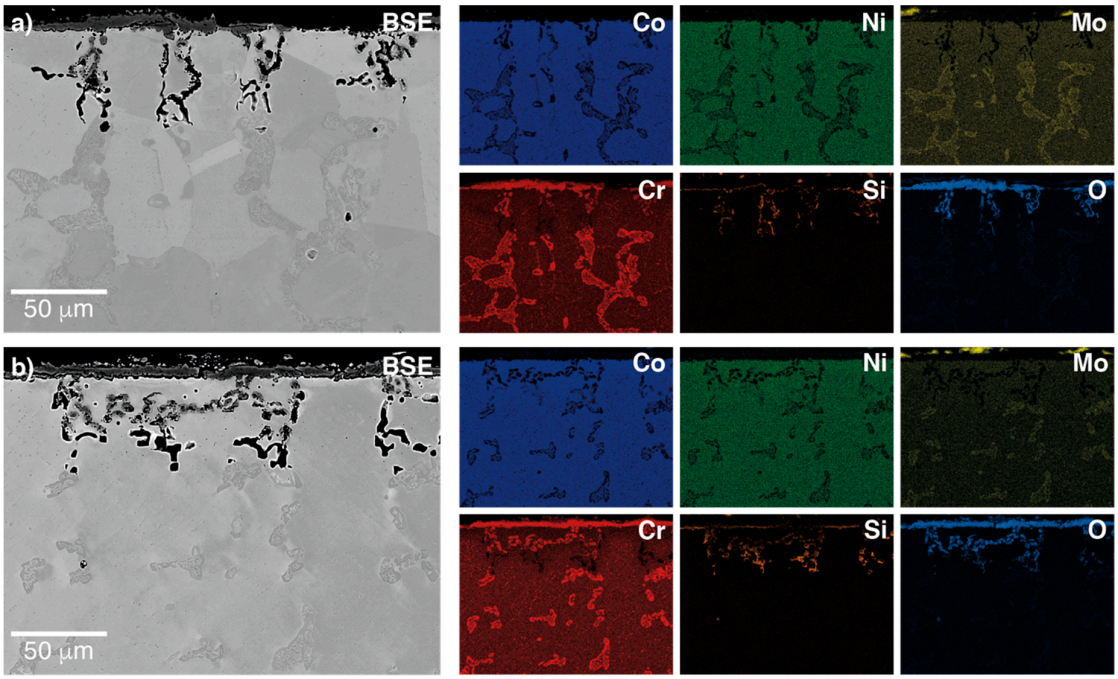

Figure 6. BSE images and corresponding Co, Ni, Mo, Cr, Si, and O EDX element distribution maps after 100 h oxidation at 1000 °C for (**a**) as-cast and (**b**) 1250 °C 10 h heat treated Co-101.

A Cr concentration gradient near the sample surfaces can be observed in the EDX elemental maps in Figure 6. This may be expected as a result of outward migration of Cr to the metal-oxide interface during oxidation. Porosity could also be observed near the alloy-oxide interface, near the carbide network, and at grain boundaries. This is likely a result of the Kirkendall effect [33] from the outward diffusion of Cr to the surface, as observed in solution heat-treatments of the Ni-Cr alloy 617 [34]. This mechanism should also be active in close proximity to the oxidising network where diffusion of Cr from the matrix to the carbide regions would be expected to occur. For this reason, Kirkendall porosity was found to extend to a similar depth as that of the oxidised carbides.

Notably, the BSE images of the oxidised samples in Figure 7 indicate the formation of secondary precipitates throughout the γ matrix. As these precipitates were not observed in the microstructure following solution heat treatment their occurrence may be attributed to relief of C supersaturation in the solid solution at 1000 °C to form intra-granular carbides. Near the metal-oxide interface of the oxidised samples, voids were observed of the same morphology and size as these intra-granular carbides, although no evidence of oxidation products was observed within them. This suggests that dissolution of these precipitates occurred with diffusional transport carrying these species away from these locations. In addition to the changes to the intra-granular carbide distribution and Cr concentrations, a noticeable increase in the fraction of ε phase was observed near the alloy surface. This could be a result of the stresses induced by the oxide scale growth [35], a phase transformation caused by the outward diffusion of γ-stabilising elements similar to that observed in thermal barrier coatings [36] and austenitic steels [37] during oxidation, or due to the higher cooling rates experienced at the surfaces of the specimen during cooling [38].

It can be seen from the Co-101 alloy microstructures that the high temperature heat-treatment, Figure 6, did not significantly reduce oxidation attack down the continuous carbide network. Despite the heat treatment being near the solidus of the alloy, the carbide network could not be fully solutioned, with only the $M_{23}C_6$ carbide being fully dissolved. This issue cannot be resolved in alloys of this type with such high C content as only limited resolutioning of the carbides is possible before the onset of incipient melting. However, alloys with lower C content, such as Stellite-21, may allow more complete dissolution of the carbide network during heat treatment.

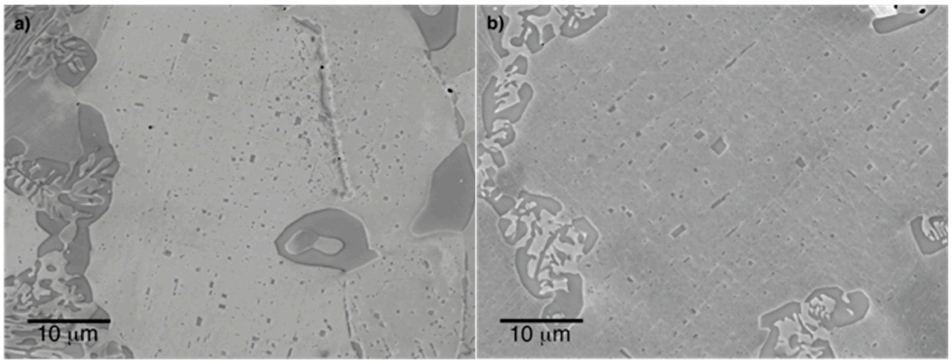

Figure 7. BSE images of the secondary carbide precipitation after oxidation testing at 1000 °C for 100 h of (**a**) as-cast and (**b**) solution heat treated Co-101 specimens.

3.4. Microstructure of Stellite-21

In order to assess the effect of partial dissolution of the carbide networks on the oxidation resistance of lower C-containing Co-based superalloys, oxidation testing was performed on samples of Stellite-21 both before and after heat treatment. This alloy was selected for its compositional similarity to Co-101 and lower C content, which is approximately half of that of Co-101.

The microstructure of Stellite-21 in various conditions has been subject to rigorous analysis in the literature [15,39] and has been shown to comprise of γ dendrites with interdendritic M_7C_3, $M_{23}C_6$, M_6C, Cr_3C_2, and σ phase [15]. SEM micrographs of the re-cast Stellite-21 investigated in this study are shown in Figure 8. Low magnification imagining (Figure 8a, revealed the microstructure to contain γ dendrites with a centre-to-centre spacing of 13–18 μm with interdendritic regions, which constituted 4% of the microstructure, as determined using image analysis. The interdendritic lamella intergrowth, Figure 8b, was similar to those observed in Co-101 (Figure 1c), although the lamellae were finer in Stellite-21.

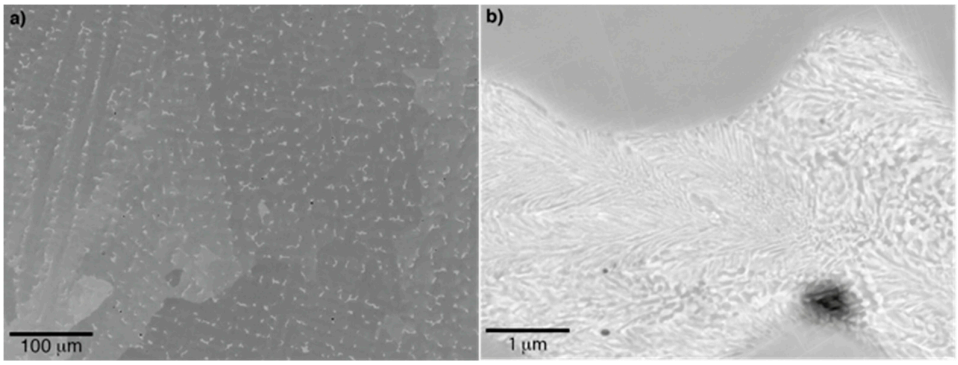

Figure 8. BSE micrographs of Stellite-21 in the as-cast state. (**a**) Low magnification image of the dendritic microstructure. (**b**) Higher magnification image of the interdendritic lamella intergrowth.

Microstructural analysis of the interdendritic lamella intergrowth using STEM EDX revealed that it comprised one phase rich in Co, Fe and Ni and the other rich in Cr and Mo, Figure 9. SADPs obtained from this region were consistent with the presence of the $M_{23}C_6$ phase.

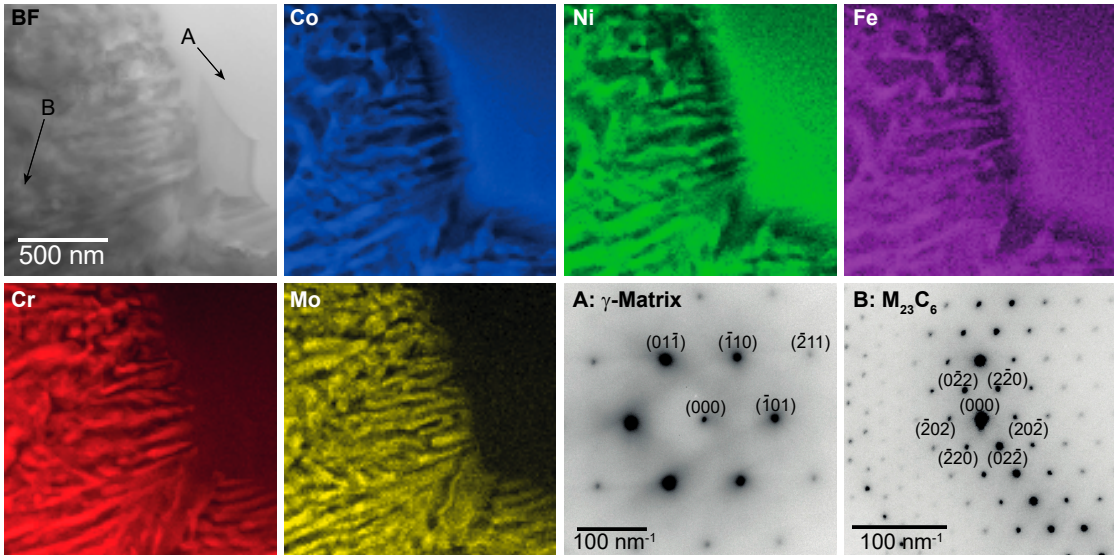

Figure 9. Bright field (BF) image of a region of interest in Stellite-21 with corresponding STEM-EDX elemental distribution maps of Co, Ni, Fe, Cr and Mo. SADPs of the regions labelled A and B in the BF image, were identified as containing the γ matrix and $M_{23}C_6$ with [111] zone axes.

DSC data acquired from Stellite-21 in the as-cast condition, shown in Figure 10, revealed endothermic events with peaks at 1252 °C and 1389 °C. These events were believed to correspond to the melting of the interdendritic and dendritic constituents respectively. As such, a heat treatment of 10 h at 1250 °C was selected for carbide modification whilst minimising the likelihood of incipient melting. The microstructure of the alloy after heat treatment showed near complete dissolution of the interdendritic constituents, Figure 11a, with only a small number of precipitates remaining, Figure 11b. This is in stark contrast to Co-101 where the majority of the carbide network remained intact after the heat treatment. In addition to the dissolution of the carbides, a significant amount of porosity could also be observed in the heat treated Stellite-21 microstructure.

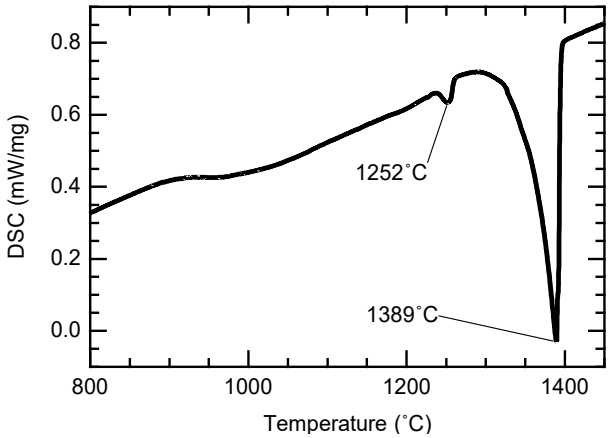

Figure 10. DSC thermogram of as-cast Stellite-21 with the two major endothermic peaks labelled.

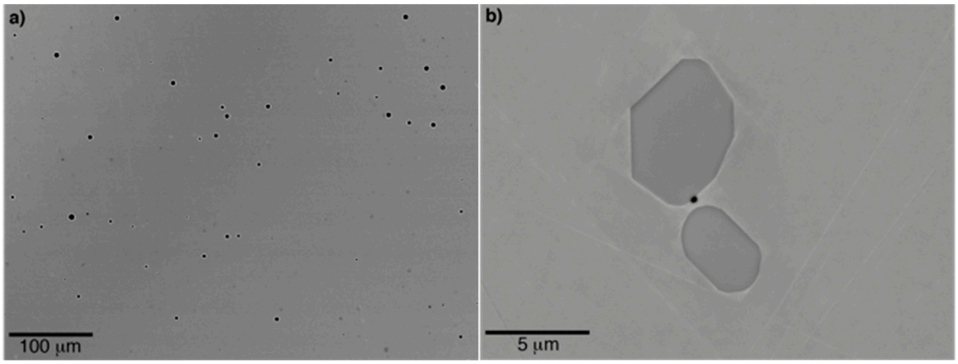

Figure 11. BSE micrographs of Stellite-21 in the 1250 °C 10 h heat-treated state. (**a**) Low magnification image of the microstructure. (**b**) High magnification images of the precipitates.

3.5. Oxidation of Stellite-21

The cross-sectional microstructures of Stellite-21 following oxidation at 1000 °C for 100 h starting from the as-cast and heat-treated states, along with their associated SEM-EDX elemental concentration maps, are shown in Figure 12. Unlike the results obtained from Co-101, which showed similar oxidation responses from the two microstructural conditions, the heat-treated Stellite-21 exhibited markedly different oxidation behaviour.

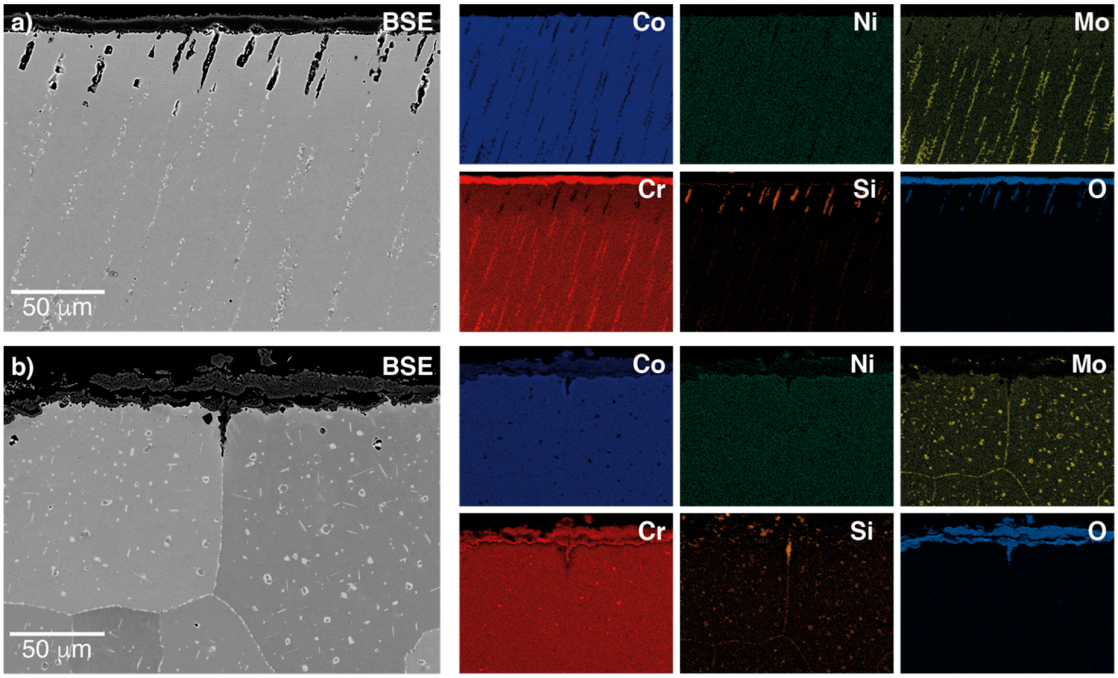

Figure 12. BSE image as well as Co, Ni, Mo, Cr, Si, and O EDX element distribution maps after 100 h oxidation at 1000 °C of (**a**) as-cast and (**b**) 1250 °C 10 h heat-treated Stellite-21.

After oxidation at 1000 °C for 100 h the as-cast material formed a continuous Cr-rich oxide layer 9 µm thick. Beneath this layer, the elongated interdendritic carbides showed evidence of extensive oxidation attack, leaving porous fissures where these oxides had resided to a depth of 50 µm. Whilst O was detected in these fissures this was not associated with clear increases in signal from either Cr or Co, as observed in the oxidation of Co-101. However, there was a significantly enriched region of Si within the fissures, possibly as a result of SiO_2 formation. As with Co-101 a Cr-depleted region

accompanied by Kirkendall porosity was observed beneath the external oxide scale and to a depth similar to that of the carbide attack. The mass gain from this oxidation test was 1.38 mg/cm^2.

At greater depths into the alloy substrate, the primary carbides displayed breakdown of the eutectic carbide structures, with the lamella structures becoming blocky, Figure 13a. This may be attributed to the prolonged exposure at elevated temperature and is not believed to be related to the oxidation process. As with Co-101, the elevated temperature exposure was also seen to induce secondary carbide precipitation localised around the primary carbide network. As the depth of oxidation attack along the interdendritic carbide networks of the as-cast Stellite-21 was similar to that of Co-101, it is clear that the reduced carbide volume fraction from the lower C content of the alloy was insufficient to significantly improve the oxidation behaviour.

The oxidised surface of the heat-treated Stellite-21 sample was seen to differ markedly from that of the as-cast condition. A surface scale between 9–20 μm thick was observed, predominately comprising a mixture of Cr and Co-rich oxides, potentially the Cr_2O_3 and Co_3O_4 spinel. This mixed oxide scale appeared to be less uniform than that formed on the as-cast sample, with evidence of porosity, spallation and varying oxide thickness. The mass gain for the heat-treated specimen following the exposure at 1000 °C for 100 h was 7.43 mg/cm^2.

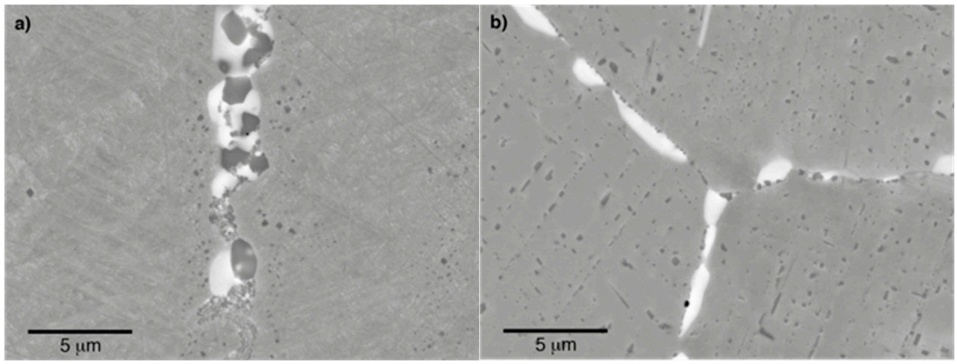

Figure 13. BSE images of the secondary carbide precipitation after oxidation testing at 1000 °C for 100 h of (**a**) as-cast and (**b**) solution heat treated Co-101 specimens.

Beneath the oxide scale of the heat-treated and oxidised Stellite-21 extensive secondary carbide precipitation, rich in Mo and Si, was observed both within the grains and along grain boundaries (Figure 13b). These carbides were not observed in the solution heat treated condition (Figure 11) and, therefore, must have developed during the exposure at 1000 °C for 100 h. Critically, the interconnectivity of these carbides was significantly lower than that of the interdendritic carbides present in the as-cast microstructure. The intragranular carbides showed very limited evidence of oxidation attack beneath the external oxide scale. This may be attributed to them being isolated from direct exposure to the atmosphere by the matrix. As a result of the carbides being more discontinuous and separated by the matrix, diffusion through the bulk is the limiting rate of oxidation of the carbides, rather than rapid oxidation along the continuous carbide networks. Whilst this led to significantly reduced intragranular oxidation attack depths, the more continuous distributions of carbides along the grain boundaries still provided a pathway for preferential oxidation attack, as can be seen between the two large grains in the BSE image in Figure 12b. The resulting fissure reached a depth of 30 μm, similar to the depth of interdendritic carbide attack in the as-cast state. This indicates that the intergranular carbides provide a route for oxidation attack akin to those of the intragranular interdendritic carbides. As with the other cases considered, Kirkendall porosity was also observed to form in close proximity to the oxidised surface.

The results of this study have shown that modification of the carbide network by heat treatment is more effective in the low C-containing Stellite-21 alloy than the high C-containing Co-101. This modification reduced the connectivity of the $M_{23}C_6$ carbide network and succeeded in eliminating preferential oxidation attack along interdendritic regions. However, grain boundary carbides still

offered a route for attack with damage depths comparable to those of the continuous interdendritic carbide networks present in the other conditions examined. More problematically, the redistribution of carbon within the material adversely affected the ability of the alloy to form a thin continuous protective oxide scale. This manifested as a greater mass gain and thicker, mixed oxide overscale for the heat-treated sample. As such, it may be desirable to consider alloys with even lower C contents or with elemental additions that form more stable intragranular carbides if oxidation resistance is to be improved through similar heat treatments. It is also critical that the effect of modifying carbide distributions in this way may adversely affect other properties, particularly tensile and creep behaviour [40–42] and careful consideration of the particular service requirements will be necessary to ensure that an appropriate balance of properties for a particular application is retained.

4. Conclusions

The effects of near-solidus heat treatment on the microstructure and oxidation resistance of two Co-based alloys with differing C content have been assessed from which the following conclusions were drawn:

(1) The long, continuous carbide networks present in the as-cast microstructures act as preferential sites for oxidation attack.

(2) The interdendritic M_7C_3 carbides in alloys with high C content (e.g., Co-101) cannot be fully solutioned and redistributed. Thus, oxidation attack along the interdendritic carbide network persists.

(3) The interdendritic carbides in alloys with lower C content (e.g., Stellite-21) can be effectively dissolved and re-precipitated. This allows the carbide continuity to be significantly decreased, thereby eliminating significant attack along the interdendritic regions. However, damage to similar depths still occurs as a result of oxidation of grain boundary carbides.

(4) The redistribution of C through heat treatments of this type adversely affected the ability of the alloy to form a compact, protective chromia layer, leading to a thicker external oxide scale and increased mass gain rates.

Author Contributions: Conceptualization and methodology, H.J.S. and N.G.J.; software, J.P.M.; investigation and formal analysis, J.P.M., K.A.C., E.J.P. and T.E.W.; validation and visualization, J.P.M. and T.E.W.; resources, H.J.S.; data curation, J.P.M.; writing—original draft preparation, J.P.M.; writing—review and editing, K.A.C., E.J.P., H.J.S. and N.G.J.; supervision, K.A.C, H.J.S. and N.G.J.; project administration, H.J.S.; funding acquisition, H.J.S. All authors have read and agreed to the published version of the manuscript.

Acknowledgments: The authors wish to thank Sue Rhodes for assistance with re-casting of the Stellite-21 samples. The underlying research data can be found at https://doi.org/10.17863/CAM.48711.

Conflicts of Interest: The authors declare no conflict of interest.

References

1. Liu, R.; Yao, M.X.; Wu, X.J. Influence of carbon content in cobalt-based superalloys on mechanical and wear properties. *J. Eng. Mater. Technol.* **2004**, *126*, 204–212.
2. Riddihough, M. Stellite as a wear-resistant material. *Tribology* **1970**, *3*, 211–215.
3. Shin, J.-C.; Doh, J.-M.; Yoon, J.-K.; Lee, D.-Y.; Kim, J.-S. Effect of molybdenum on the microstructure and wear resistance of cobalt-base Stellite hardfacing alloys. *Surf. Coat. Technol.* **2003**, *166*, 117–126.
4. Pettit, F.S.; Meier, G.H. Oxidation and Hot Corrosion of Superalloys. In Proceedings of the Fifth International Symposium on Superalloys, Seven Springs Mountain Resort, Champion, PA, USA, 7–11 October 1984; pp. 651–687.
5. Zhang, X.Z., Liu, R., Chen, K.Y.; Yao, M.X. Pitting corrosion characterization of wrought Stellite alloys in Green Death Solution with immersion test and extreme value analysis model. *J. Mater. Eng. Perform.* **2014**, *23*, 1718–1725.
6. Rosalbino, F.; Scavino, G. Corrosion behaviour assessment of cast and HIPed Stellite 6 alloy in a chloride-containing environment. *Electrochim. Acta* **2013**, *111*, 656–662.
7. Yao, M.X.; Wu, J.B.C.; Xie, Y. Wear, corrosion and cracking resistance of some W- or Mo-containing Stellite hardfacing alloys. *Mater. Sci. Eng. A* **2005**, *407*, 234–244.

8. Sims, C.T.; Stoloff, N.S.; Hagel, W.C. *Superalloys II*, 2nd ed.; John Wiley & Sons: Hoboken, NJ, USA, 1987.
9. Donachie, M.J.; Donachie, S.J. *Superalloys*: *A Technical Guide*, 2nd ed.; ASM International: Philadelphia, PA, USA, 2002.
10. Coutsouradis, D.; Davin, A.; Lamberigts, M. Cobalt-based superalloys for applications in gas turbines. *Mater. Sci. Eng.* **1987**, *88*, 11–19.
11. Steinmetz, P.; Rapin, C. Corrosion of high temperature alloys by molten glass. *Mat. Sci. Forum* **2001**, *369–372*, 865–827.
12. Zaman, H.A.; Sharif, S.; Kim, D.-W.; Idris, M.H.; Suhaimi, M.A.; Tumurkhuyag, Z. Machinability of Cobalt-based and Cobalt Chromium Molybdenum Alloys—A Review. *Procedia Manuf.* **2017**, *11*, 563–570.
13. Helmink, R.C. The golden age of cast structural superalloys. In Proceedings of the Eighth International Symposium on Superalloy 718 and Derivatives, Pittsburgh, PA, USA, 28 September–1 October 2014; pp. 171–180.
14. Birks, N.; Meier, G.H.; Pettit, F.S. *Introduction to the High Temperature Oxidation of Metals*, 2nd ed.; Cambridge University Press: Cambridge, UK, 2006.
15. Sullivan, C.P.; Donachie, M.J.; Morral, F.R. *Cobalt-Base Superalloys-1970*; Centre d'Information du Cobalt: 1970.
16. Jiang, W.H.; Yao, X.D.; Guan, H.R.; Hu, Z.Q.; Jiang, W.H. Secondary carbide precipitation in a directionally solified cobalt-base superalloy. *Metall. Mater. Trans. A* **1999**, *30*, 513–520.
17. Di Martino, J.; Rapin, C.; Berthod, P.; Podor, R.; Steinmetz, P. Corrosion of metals and alloys in molten glasses. Part 2: Nickel and cobalt high chromium superalloys behaviour and protection. *Corros. Sci.* **2004**, *46*, 1865–1881.
18. Gabb, T.P.; Telesman, J.; Hazel, B.; Mourer, D.P. The effects of hot corrosion pits on the fatigue resistance of a disk superalloy. *J. Mater. Eng. Perform.* **2009**, *19*, 77–89.
19. Di Martino, J.; Rapin, C.; Berthod, P.; Podor, R.; Steinmetz, P. Corrosion of metals and alloys in molten glasses. Part 1: Glass electrochemical properties and pure metal (Fe, Co, Ni, Cr) behaviours. *Corros. Sci.* **2004**, *46*, 1849–1864.
20. Radu, I.; Llewellyn, D.Y. Tribological behavior of Stellite 21 modified with yttrium. *Wear* **2004**, *257*, 1154–1166.
21. Sims, C.T. A contemporary view of cobalt-base alloys. *JOM* **1969**, *12*, 27–42.
22. Berthod, P. High temperature properties of several chromium-containing Co-based alloys reinforced by different types of MC carbides (M = Ta, Nb, Hf and/or Zr). *J. Alloys Compd.* **2009**, *481*, 746–754.
23. Berthod, P. Looking for New Polycrystalline MC-Reinforced Cobalt-Based Superalloys Candidate to Applications at 1200 degrees C. *Adv. Mater. Sci. Eng.* **2017**, 4145369, doi:10.1155/2017/4145369.
24. Schneider, C.A.; Rasband, W.S.; Eliceiri, K.W. NIH Image to ImageJ: 25 years of image analysis. *Nat. Methods* **2012**, *9*, 671–675.
25. Hitzenberger, C.; Karnthaler, H.P. Weak-beam TEM study of the h.c.p. to f.c.c. martensitic phase transformation lamellae in CoNi. *Philos. Mag. A* **1991**, *64*, 151–163.
26. Tawancy, H.M. Microstructural Characterization of the face-centered cubic-to-hexagonal close-packed transition in a cobalt-base alloy and its effect on mechanical strength. *Metallogr. Microstruct. Anal.* **2018**, *7*, 288–297.
27. Giacchi, J.V.; Morando, C.N.; Fornaro, O.; Palacio, H.A. Microstructural characterization of as-cast biocompatible Co-Cr-Mo alloys. *Mater. Charact.* **2011**, *62*, 53–61.
28. Park, J.B.; Jung, K.-H.; Kim, K.M.; Son, Y.; Lee, J.I.; Ryu, J.H. Microstructure of As-cast Co-Cr-Mo Alloy Prepared by Investment Casting. *J. Korean Phys. Soc.* **2018**, *72*, 947–951.
29. Ahmed, R.; de Villiers Lovelock, H.L.; Faisal, N.H.; Davies, S. Structure-property relationships in a CoCrMo alloy at micro and nano-scales. *Tribol. Int.* **2014**, *80*, 98–114.
30. Liu, R.; Yao, J.H.; Zhang, Q.L.; Yao, M.X.; Collier, R. Microstructures and hardness/wear performance of high-carbon Stellite Alloys Containing molybdenum. *Metall. Mater. Trans. A* **2015**, *46*, 5504–5513.
31. Krell, J.; Röttger, A.; Theisen, W. Comprehensive investigation of the microstructure-property relationship of differently manufactured Co-Cr-C alloys at room and elevated temperatures. *Wear* **2020**, *444–445*, 203138.
32. Taylor, R.N.J.; Waterhouse, R.B. A study of the ageing behaviour of a cobalt based implant alloy. *J. Mater. Sci.* **1983** *18*, 3265–3280.
33. Smigelskas, A.D. Zinc diffusion in alpha brass. *Trans. AIME* **1947**, *171*, 130–142.

34. Ennis, P.J.; Quadakkers, W.J.; Schuster, H. The effect of selective oxidation of chromium on the creep strength of alloy 617. *J. Phys. IV* **1993**, *3*, C9-979-C9-986.
35. Huntz, A.M.; Schütze, M. Stresses generated during oxidation sequences and high temperature fracture. *Mater. High Temp.* **1994**, *12*, 151–161.
36. Cáceres-Díaz, L.A.; Alvarado-Orozco, J.M.; Ruiz-Luna, H.; García-Herrera, J.E.; Mora-García, A.G.; Trápaga-Martinez, G.; Arroyave, R.; Muñoz-Saldaña, J. Study of the Isothermal Oxidation Process and Phase Transformations in B2-(Ni,Pt)Al/RENE-N5 System. *Metals* **2016**, *6*, 208.
37. Susan, D.F.; Knorovsky, G.A.; Robino, C.V.; Michael, J.R.; Rodriguez, M.A.; Perricone, M.J. Surface alloy depletion and martensite formation during glass to metal joining of austenitic stainless steels. *Sci. Technol. Weld. Join.* **2012**, *17*, 321–332.
38. Weißensteiner, I.; Petersmann, M.; Erdely, P.; Stark, A.; Antretter, T.; Clemens, H.; Maier-Kiener, V, Deformation-induced phase transformation in a Co-Cr-W-Mo alloy studied by high-energy X-ray diffraction during in-situ compression tests. *Acta Mater.* **2019**, *164*, 272–282.
39. Liu, R.; Yao, J.H.; Zhang, Q.L.; Yao, M.X.; Collier, R. Relations of chemical composition to solidification behavior and associated microstructure of Stellite Alloys. *Metallogr. Microstruct. Anal.* **2015**, *4*, 146–157.
40. Kontis, P.; Li, Z.; Segersäll, M.; Moverare, J.J.; Reed, R.C.; Raabe, D.; Gault, B. The role of oxidized carbides on thermal-mechanical performance of polycrystalline superalloys. *Metall. Mater. Trans. A* **2018**, *49*, 4236–4245.
41. Gui, W.; Zhang, H.; Yang, M.; Jin, T.; Sun, X.; Zheng, Q. Influence of type and morphology of carbides on stress-rupture behavior of a cast cobalt-base superalloy. *J. Alloys Compd.* **2017**, *728*, 145–151.
42. Jiang, W.H.; Guan, H.R.; Hu, Z.Q. Development of a heat treatment for a directionally solidified cobalt-base superalloy. *Metall. Mater. Trans. A* **1999**, *30*, 2251–2254.